Radiative Muon Capture on O, Al, Si, Ti, Zr, and Ag

P. C. Bergbusch,(1) D. S. Armstrong,(2) M. Blecher,(3) C. Q. Chen,(4)
B. C. Doyle,(5) T. P. Gorringe,(5) P. Gumplinger,(4) M. D. Hasinoff,(1)
G. Jonkmans,(6,*) J. A. Macdonald,(4) J-M. Poutissou,(4) R. Poutissou,(4)
C.N. Sigler,(3) and D.H. Wright,(4)

(1) *University of British Columbia, Vancouver, British Columbia, Canada V6T 1Z5*
(2) *College of William and Mary, Williamsburg, Virginia 23187*
(3) *Virginia Polytechnic Institute and State University, Blacksburg, Virginia 24061*
(4) *TRIUMF, Vancouver, British Columbia, Canada V6T 2A3*
(5) *University of Kentucky, Lexington, Kentucky 40506*
(6) *Université de Montréal, Montréal, Quebec, Canada H3C 3J7*

(October 13, 1998)

The photon spectra from radiative muon capture (RMC) on O, Al, Si, Ti, Zr, and Ag have been measured for photon energies greater than 57 MeV using a cylindrical pair spectrometer at the TRIUMF cyclotron. Values of R_γ, the ratio of the radiative rate for photon energies above 57 MeV, to the non-radiative rate, are 1.67±0.17, 1.41±0.11, 2.09±0.23, 1.30±0.12, 1.31±0.14, and 1.12±0.13, respectively, in units of 10^{-5}. The Al/Si rate difference confirms an earlier result. The Ti/Ca rate difference and the rate suppression in Zr and Ag are new results which confirm that the RMC rate is a much smoother function of neutron excess than of atomic number. This suggests that Pauli blocking is relatively more important for radiative capture than for non-radiative capture. The value of the ratio of the induced weak pseudoscalar to axial coupling constants, g_p/g_a, for O was found to be $6.4^{+1.0}_{-1.1}$, in good agreement with the partially conserved axial current hypothesis (PCAC). For the other nuclei studied, large model-dependences or a lack of detailed RMC calculations made tests of PCAC difficult.

23.40.Hc, 11.40.Ha, 27.40.+z, 27.50.+e

I. INTRODUCTION

The form of the weak interaction at low energies when hadrons are involved can be studied via semi-leptonic processes. Fermi first described such processes in terms of a contact interaction between weak currents [1]. For a semi-leptonic process, the weak current is written as J^α and may be decomposed into leptonic and hadronic parts:

$$J_\alpha(x) = J^l_\alpha(x) + J^h_\alpha(x). \tag{1}$$

The experimental data on a wide range of leptonic and semi-leptonic processes indicate that the lepton fields enter the weak interaction in a purely $V - A$ (vector $-$ axial vector) form as expected in the Standard Model. The weak hadronic current is less well-known, but can be written in a general $V - A$ form in terms of Lorentz covariants, hadronic fields, and form factors. The form factors account for the composite structure of hadrons, and include the familiar vector and axial vector form factors, F_V and F_A, as well as the "induced" weak magnetic, scalar, pseudoscalar, and tensor form factors, F_M, F_S, F_P, and F_T [2]. With the exception of F_P, the form factors are either identically zero or weak functions of q^2, so it is useful to define a set of coupling constants $g_{i=v,a,m,s,p,t}$, which are given by the form factors evaluated at fixed q^2.

Experimental and theoretical constraints on the weak form factors include time reversal invariance, G parity invariance, the conserved vector current hypothesis (CVC), and β-decay of the neutron. These constraints leave g_p the coupling constant with the largest experimental uncertainty. Early predictions [3,4] of the value of g_p were made using the partially conserved axial current hypothesis (PCAC). The more recent chiral perturbation approach [5] provides the best theoretical value, $g_p(q^2 = -0.88m_\mu^2) = 6.7g_a(0) = 8.44 \pm 0.23$.

Muon capture processes are well-suited to the measurement of g_p because they involve large momentum transfers and axial vector currents. The process of radiative muon capture (RMC) on the proton

$$\mu^- + p \rightarrow n + \nu_\mu + \gamma, \tag{2}$$

*Present address: Institut de Physique, Université de Neuchâtel, CH-2000, Neuchâtel, Switzerland.

has an easily detected final state particle (the photon), and the RMC photon energy spectrum is directly related to g_p. Also, because it is the high energy RMC photons that are experimentally observed, the momentum transfer is close to the pion pole resulting in an enhancement of the RMC amplitude by a factor of ~ 3 over ordinary muon capture (OMC). However, RMC is a rare process and the first measurement of the branching ratio on the proton was performed only recently [6,7]. The ratio of RMC to OMC branching ratios at the high energy end of the RMC photon spectrum is $\sim 10^{-5}$ and the partial branching ratio in H is 2.1×10^{-8}. Therefore, measurement of RMC requires a careful assessment of backgrounds.

Nuclear RMC is easier to measure than the elementary process because the rate for muon capture goes as Z^4_{eff}, where Z_{eff} is an effective nuclear charge. However, the g_p term in the RMC amplitude is sensitive to pion exchange, so modifications to the pion propagator in the nuclear medium, nucleon polarizability, short-range nucleon-nucleon correlations, and medium modifications of the pion lifetime, may modify the value of g_p in a nucleus. Furthermore, due to the experimental difficulty in resolving final nuclear states of the RMC process, nuclear RMC measurements are typically inclusive, which adds complication due to the necessary nuclear structure calculations.

Nuclear medium effects common to RMC and OMC can be reduced if one observes the ratio of RMC to OMC branching ratios. The partial ratio of RMC to OMC rates for photons with $E_\gamma > 57$ MeV is defined as R_γ and has been calculated as a function of g_p, along with the RMC photon spectrum, for several nuclei using various models. Nevertheless, large model dependences [8] make it unclear whether all nuclear medium effects are removed in this way.

In the present experiment two nuclear medium effects were studied: a neutron excess effect between nuclear neighbors and a quenching of the RMC rate with increasing Z. Differential and integrated RMC photon spectra were measured for six different nuclear targets with naturally occurring isotopic abundances. The neutron excess effect was studied in Al and Si targets in order to confirm an effect seen earlier [9]. Ti was chosen for comparison with previous Ca results [8,10–13] to see if a neutron excess effect might also be present there. Zr and Ag were chosen in order to investigate the trend of decreasing R_γ with increasing atomic number. Finally, an O target was chosen in order to compare with earlier O results from PSI [10,14] and TRIUMF [8].

II. EXPERIMENTAL SETUP

Negatively charged muons from the M9A beamline at TRIUMF [15] were stopped in various targets and then captured by target nuclei. A small percentage of the captures produced photons which were detected by their conversion into e^+e^- pairs in a cylindrical Pb sheet and subsequent tracking in a cylindrical drift chamber. A full description of the entire RMC photon spectrometer, its operation, and the photon and particle triggers used, is given in Ref. [16].

Six nuclear targets, all with naturally occurring isotopic abundances, were used in various states and forms. Their dimensions are listed in Table I. The O target consisted of liquid D_2O in a thin polyethylene bag whose cylindrical shape was defined by a lucite ring and mono-filament fishing line. It was supported in the center of the spectrometer by polystyrene foam. Liquid was chosen for its sufficient muon stopping power, and D_2O was used instead of H_2O because the radiative pion capture (RPC) photon background arising from the charge exchange reaction, $\pi^- + p \rightarrow n + \pi^0 \rightarrow 2\gamma$, is three orders of magnitude smaller for the deuteron than it is for the proton [17]. Also, RMC on the deuteron is insignificant compared to that in O.

The Si target consisted of granular Si in a polypropylene container held at the center of the spectrometer by polystyrene foam. The Al, Zr, and Ag targets consisted of several thin, self-supporting metallic plates, and the Ti target of metallic shavings, all kept in place by polystyrene foam holders. The motivation for using grains, plates, and shavings, instead of solid targets, was to reduce photon conversion in the target.

A C target, used for calibration of the spectrometer, was composed of a single disk of graphite, 15.4 cm in diameter and 1.9 cm thick.

Each target was located 17 cm downstream of the beam counters and was surrounded by two concentric cylinders of scintillation counters. A 0.635 cm thick veto scintillator was placed immediately downstream of the target so that muons not stopping in the target could be vetoed. An incident muon was defined by

$$BM1 \cdot BM2 \cdot BM3 \cdot BM4 \cdot RF_\mu \cdot \overline{V + A + A'} \cdot \overline{MV} \tag{3}$$

where $BM1 \cdot BM2 \cdot BM3 \cdot BM4$ is the fourfold beam counter coincidence, RF_μ is the muon time-of-flight signal derived from the cyclotron, $\overline{MV}$ is the absence of the master veto (computer busy, low beam rate or equipment faults), and $\overline{V + A + A'}$ is the absence of a hit in the scintillator layers surrounding the target or in the veto scintillator downstream of the target.

III. DATA ANALYSIS

A. Event Selection

Event selection criteria based on track fit quality, event topology, and kinematics, were applied to the spectrometer data. While these cuts are briefly summarized here, a thorough discussion of them can be found in Refs. [7,9]. The "Cstrobe" cut rejected photons in which none of the scintillators immediately outside of the Pb converter cylinder fired. This cut removed photons which did not arise from pair production in the converter. The veto cut rejected photons which were accompanied by hits in the three layers of scintillators immediately inside the Pb converter cylinder, and which were in time with the candidate photon. This cut rejected events such as bremsstrahlung, in which charged particles accompanied the photon. The tracking cut selected photons based on e^+ and e^- track fitting parameters. These parameters included the number of points used in the fit, the χ^2 of the fit, and the distance from the center of the spectrometer to the apex of the track. This cut suppressed non-gaussian tails in the spectrometer response function, and rejected some bremsstrahlung and cosmic ray photons. The photon cut selected events based on the topology of the observed photon. Useful parameters included the quality and opening angle of the e^+e^- vertex and its proximity to the Pb converter, the component along the beam axis (z) of the distance of closest approach between the extrapolated path of the photon and the center of the spectrometer, and the difference in the z components of the e^+ and e^- momenta. This cut removed photons which originated from locations outside of the nuclear target. The false photon cut rejected photons constructed from fortuitous combinations of Michel electron and conversion positron tracks in the drift chamber. Prompt photons were removed by the prompt cut and photons induced by cosmic rays were removed by the cosmic cut.

B. Backgrounds

Nearly all the events surviving the above cuts are true photons, but most of them are due to backgrounds such as bremsstrahlung, radiative pion capture (RPC) and to a much lesser extent, cosmic rays. Branching ratios for RPC ($\sim 2 \times 10^{-2}$) are three orders of magnitude larger than for RMC ($\sim 10^{-5}$) and hence present a potentially serious background. This was effectively removed by time-of-flight separation of pions in the beam and rejection of photons with prompt timing. The RPC rejection factor can be estimated by comparing the sample RMC spectrum after all cuts to the RPC on C spectrum which was taken as a spectrometer calibration. The peak of the RPC spectrum is near 110 MeV while the endpoint of the RMC spectrum is around 100 MeV. By attributing to RPC all events in the RMC spectrum above 100 MeV, an upper bound on the prompt event rejection factor was found. Combining the pion content of the separated beam (10^{-3}) with a prompt event rejection factor typical for the RMC targets (2×10^{-7}) yielded a total RPC suppression of 2×10^{-10}.

Due to the large muon stopping rate in the spectrometer, bremsstrahlung of Michel electrons and radiative muon decay (RMD) presented a large, unavoidable background with a kinematic endpoint of 53 MeV. These events were removed by rejecting all photons with energies less than 57 MeV (to allow for finite spectrometer energy resolution). The remaining muon decay background above 57 MeV, due to muon binding effects and any high-energy tail in the spectrometer response, was estimated by Monte Carlo simulations to be significant only for the O target ($\sim$0.8%; for the other targets it is $<$0.2%). These contaminations were consistent with the number of (non-RMC) photons observed above 100 MeV.

As cosmic rays enter the spectrometer they can cause background photons from electromagnetic showers. These photons were removed when an accompanying charged track was recorded in the cosmic ray scintillator/drift chamber veto layer or when hits were observed in the scintillation counters which were near the Pb converter and opposite the photon vertex. The cosmic ray background remaining after hardware and software cuts was measured to be 0.4 $\pm$ 0.1 photons/day in the energy range of interest (57-100 MeV) [7] and this was at least in part due to cosmic ray neutrons which undergo hadronic production of π^0's in the spectrometer magnet. Using the livetimes of the RMC data collection periods for the targets considered here, this background was determined to be 0.04% for O and $\leq$ 0.02% for all other targets.

The O and Si measurements required "empty" target runs in order to remove photons originating in the target containers. In these two cases the properly normalized empty container spectra were subtracted from the full container spectra to get the final spectra. The fraction of the observed number of photons which originate in the target container is given by f_{empty}, the ratio of the number of photons per incident muon in an empty container run, to the number of photons per muon in a full container run. Also included in f_{empty} is a factor which takes into account the differing fraction and distribution of muons stopping in the container when it is full or empty. This factor was determined by a Monte Carlo simulation of the known muon beam and target geometry. As indicated in the Appendix, f_{empty} is a small correction, 2.2% for O and 4.6% for Si.

The photon spectrum obtained from the Si target, at various stages in the above cuts, is shown in Figs. 1 and 2. The final photon spectrum, shown in Fig. 3, is almost entirely due to RMC in Si, with a few non-RMC photons at high energy (>100 MeV).

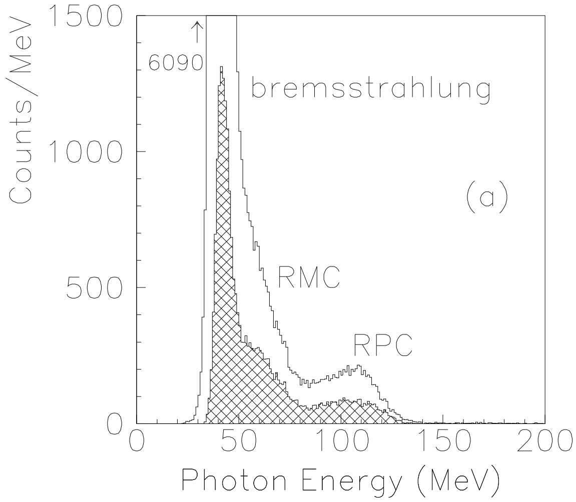

FIG. 1. Photon spectrum from μ^- on Si after veto, Cstrobe and tracking cuts (unshaded) and after photon cuts (shaded). There are no photons below $\sim$30 MeV because the spectrometer photon acceptance goes to zero at these low energies.

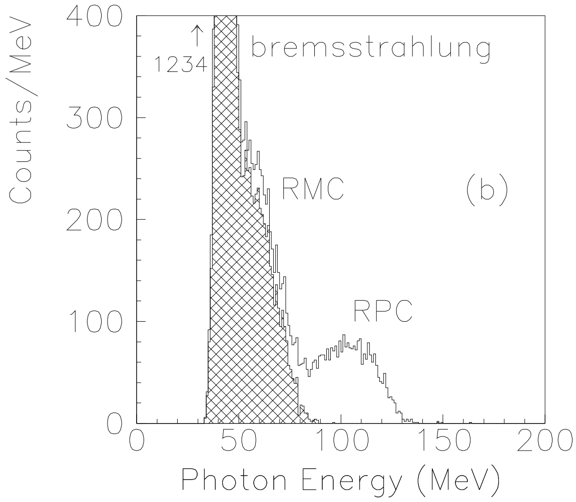

FIG. 2. Photon spectrum from μ^- on Si after veto, Cstrobe, tracking, photon and cosmic cuts (unshaded) and after prompt cuts (shaded).

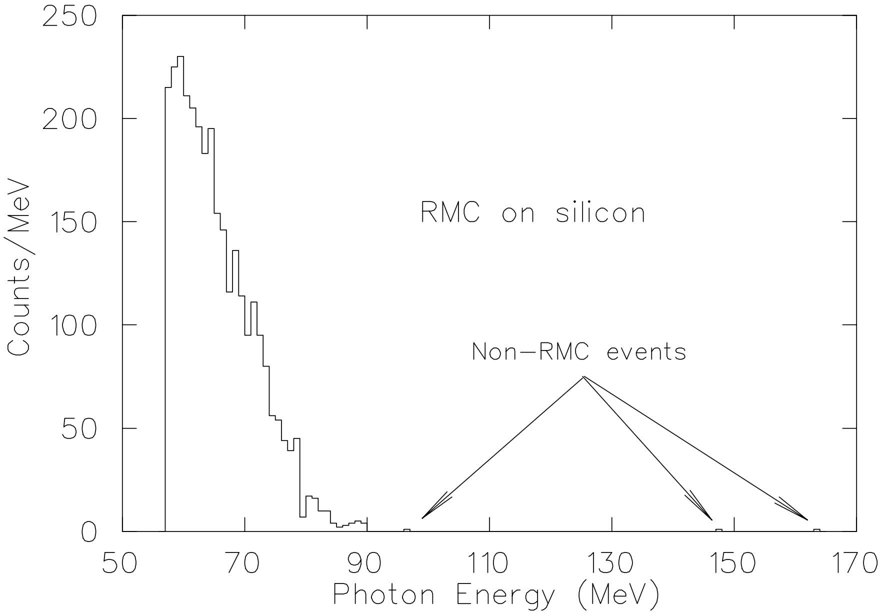

FIG. 3. Photon spectrum from μ^- on Si after all software cuts. The bremsstrahlung and RPC photon contributions have been eliminated, as seen by comparison with Figs. 1 and 2. The sharp edge at 57 MeV is due to the energy cut used to remove bremsstrahlung photons.

C. Counting RMC photons

The true number of RMC photons above 57 MeV is related to the observed number of RMC photons above 57 MeV by

$$N^{true}_{\gamma>57} = \frac{N^{obs}_{\gamma>57} \cdot F}{\epsilon_v \cdot \epsilon_{cs} \cdot \epsilon_{tr} \cdot \epsilon_{ph} \cdot \epsilon_{fp} \cdot \epsilon_c \cdot \epsilon_p \cdot A_{av}}. \tag{4}$$

where the ϵ_i are the efficiencies of the veto, Cstrobe, tracking, photon, false photon, cosmic, and prompt cuts for passing valid RMC photon events, and A_{av} is the average photon acceptance of the spectrometer weighted by the RMC spectrum shape from 57 MeV up to the RMC endpoint. F is a normalization constant described below. The product $A_{av} \cdot \epsilon_{tr} \cdot \epsilon_{ph}$ was determined as follows: the muon stopping distribution in the target was determined by a Monte Carlo simulation of the muon beam [18,19]; photons from a theoretical RMC spectrum were propagated isotropically from this stopping distribution into the spectrometer whose simulated response function was checked against a known RPC spectrum; the simulated photon spectrum generated in this way was analyzed using the above tracking and photon cuts. The number of photons surviving analysis, compared to the original number of photons generated from the target, gave $A_{av} \cdot \epsilon_{tr} \cdot \epsilon_{ph}$ for a given theoretical input RMC photon spectrum and target. This approach differed somewhat from previous nuclear RMC measurements at TRIUMF [9] done with the same spectrometer, in which its response and acceptance were determined analytically, and target-dependent effects (e.g., photon absorption) were taken into account separately. Because the simulated data contained only RMC photons, and did not take all detector inefficiencies into account, the remaining efficiencies in Eq. (4) were determined by measuring the effects of the software cuts on prompt (RPC) photons in the non-prompt (RMC) data. Their values are listed for each target in the Appendix.

The calibration of the spectrometer (i.e., the normalization of the acceptance to a well-known radiative process) was achieved by comparing simulated and measured RPC photon spectra from C, where the simulated spectrum was obtained using the energy distribution of Perroud *et al.* [20]. At the beginning and/or end of each experimental running period for a target, the beam was switched from μ^- to π^-, and RPC on C data was taken. This RPC data was analyzed in the same way as the RMC data, with the differing geometries of the C and RMC targets taken into account. The resulting branching ratio of RPC on C was then compared to the weighted average of three previous, mutually consistent branching ratio measurements [20,21], $(1.83 \pm 0.06)\%$. The ratio of the value measured in the present experiment to the average of the previous measurements, gave the factor F. The value of F, listed in the Appendix, is different from 1.0. This indicates that some spectrometer inefficiencies might have been missed in the simulation used to determine the average acceptance A_{av}, or that the true RPC branching ratio differs from 1.83 %.

The accuracy of the muon stopping distributions determined by Monte Carlo simulations was verified by comparing the simulated and measured fraction of beam muons stopping in each target. The good agreement between the shapes of the simulated and measured RPC on C photon spectra, shown in Fig. 4, and the nearness of F to 1.0 gave confidence in the acceptance and calibration determinations. The uncertainty in the acceptance depended on the form of the RMC photon spectrum and the shape of the μ stopping distribution used in the Monte Carlo simulation. When the spectrum was taken bin by bin from theory, the uncertainty was found by varying the muon stopping distribution in the target.

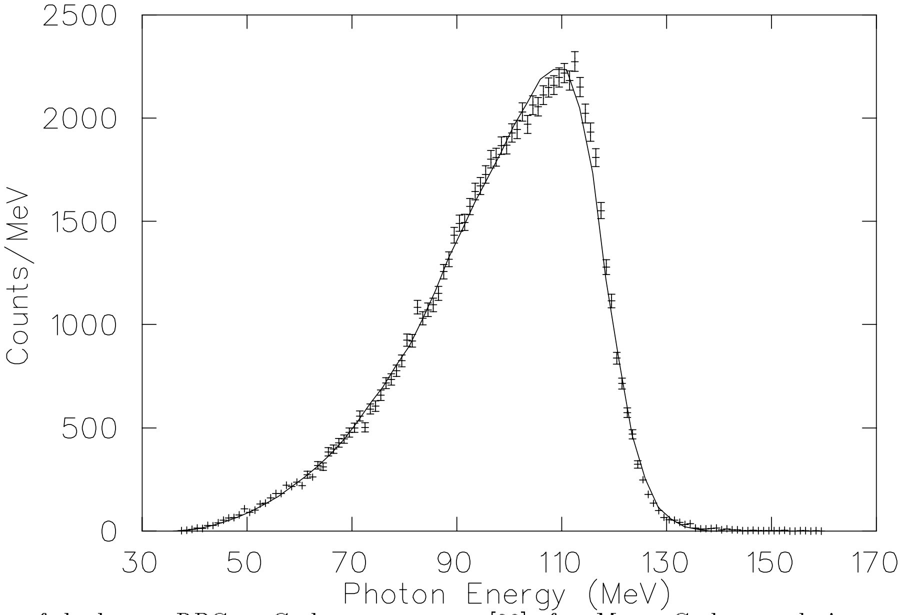

FIG. 4. Comparison of the known RPC on C photon spectrum [20] after Monte Carlo convolution and software cuts (solid line), to the RPC on C photon spectrum measured in the present experiment (error bars). The Monte Carlo spectrum has been normalized to have the same total number of counts as the measured spectrum.

Photons were generated from two extreme stopping distributions: a point source at the center of the target and a distribution uniform throughout the target. This was done explicity for the Al, Si, and C targets, and the resulting variation in the acceptance was found to be $\leq 2\%$. An uncertainty of 2% was then applied to the acceptance for the other targets. Because these two extremes in the muon stopping distribution are unrealistic, the uncertainty in the acceptance is over- rather than under-estimated.

Use of an analytic form of the RMC photon spectrum in which the maximum photon energy is a variable parameter contributed an additional uncertainty to the absolute photon acceptance. This uncertainty was bounded by evaluating the acceptance at the upper and lower limits of the maximum photon energy.

D. Counting μ^- and π^- stops

The true number of muon stops is given by

$$N_{stops}^{true} = N_{stops}^{obs} \cdot C_{bm} \cdot C_{sim} \cdot C_o \cdot C_u \cdot C_m \cdot C_{md} \tag{5}$$

where N_{stops}^{obs} is the number of times the incident muon definition as given in Eq. (3), was satisfied. The factors C_i are defined below and their measured or calculated values for each target are given in the Appendix.

Missed stops due to inefficiencies in the beam counters were corrected by C_{bm}. The inefficiency of the veto counter was not important because both the muon stopping fraction in the targets ($\sim 96\%$) and the efficiency of the veto counter ($\sim 97\%$) were large. The factor C_{sim} was determined by a Monte Carlo beam simulation and corrects for μ^- stops which occurred in the target container or the fourth beam counter, and not in the target material itself. C_o corrects for the over-counting of μ^- stops due to e^- in the beam. C_u corrects for under-counting of μ^- stops due to μ^- with incorrect timing with respect to the cyclotron rf. The correction C_m accounts for multiple particles per beam burst, in which one or more muons could be missed due to another muon arriving nearby in time. The value of

C_{md}, calculated using a Monte Carlo simulation, accounts for situations in which e^-'s from Michel decay could have vetoed an otherwise valid μ^- stop by hitting the downstream veto counter, or added a spurious μ^- stop by returning to fire all four beam counters in coincidence with the rf time.

For the RPC data, corrections to the observed number of incident pions were analogous to those for the observed number of incident muons, except that RF_μ in Eq. (3) was replaced by RF_π, and C_{md} in Eq. (5) was replaced by C_{pd}. Some pions passed through the beam counters but decayed before reaching the target, thus falsely indicating a stopped pion. The factor C_{pd} corrected for this and was determined with a Monte Carlo simulation.

The number of true pion stops is then

$$N_{\pi^-}^{true} = N_{\pi^-}^{obs} \cdot C_{bm} \cdot C_{sim} \cdot C_o \cdot C_u \cdot C_m \cdot C_{pd}. \tag{6}$$

E. Determination of R_γ and g_p/g_a

The detector acceptance depends on the photon energy, so the determination of the experimental branching ratio R_γ (and g_p/g_a) requires that model RMC spectra be convoluted with the detector response before comparison with the data. Two methods were used to accomplish this. The first, or "integral", method was used when a detailed calculation of the nuclear RMC response was available for the nucleus in question or for nuclei nearby in Z. This was the case for O, Ti, Zr, and Ag. Using g_p/g_a as an input, the theoretical RMC spectrum was calculated. This spectrum was then convoluted with the spectrometer response function as stored in the Monte Carlo simulation. Summing the convoluted spectrum above 57 MeV and multiplying by the true number of muon captures yielded the predicted number of photons as a function of g_p/g_a. A simple polynomial was then fitted to this function and the intersection of the polynomial with the observed number of photons above 57 MeV gave the measured value of g_p/g_a. A similar procedure was followed with the branching ratio R_γ used as the independent variable.

The second, or "shape", method was used for all targets. It uses the "closure" approximation of nuclear RMC, in which the final state nucleus is assigned an average excitation energy E_{av}, and the nuclear RMC matrix element is evaluated at this transition energy. Theoretical spectra are fitted to experimental spectra by treating E_{av} and g_p as free parameters. Various authors [22–27] have calculated RMC branching ratios and spectra in the closure approximation, but the extracted values of g_p are extremely sensitive to E_{av}. Therefore this model was *not* used in the present analysis to determine values of g_p. However, a closure RMC spectral shape [28,29],

$$\frac{d\Lambda(E_\gamma)}{dE_\gamma} \propto (1 - 2x + 2x^2)x(1-x)^2, \tag{7}$$

was simply used as a convenient, representative RMC photon spectrum in order to calculate values of R_γ. Here $d\Lambda(E_\gamma)/dE_\gamma$ is the physical RMC photon spectrum per muon capture and $x = E_\gamma/k_{max}$, where k_{max} is the maximum RMC photon energy. k_{max} and its uncertainty were found by fitting the simulated closure spectrum to measured RMC spectra. By definition,

$$R_\gamma = \int_{57} dE_\gamma \frac{d\Lambda(E_\gamma)}{dE_\gamma}. \tag{8}$$

As in the integral method, the physical RMC spectrum was convoluted with the spectrometer response function $A(E_\gamma, E)$ and the average acceptance A_{av}/F was found:

$$R_\gamma \cdot A_{av}/F = \int_{57} dE \int dE_\gamma A(E_\gamma, E) \frac{d\Lambda(E_\gamma)}{dE_\gamma}. \tag{9}$$

$A(E_\gamma, E)$ is the probability of a photon of energy E_γ being detected and reconstructed at an energy E. The measured photon energy spectrum, $dN_\gamma(E)/dE$, is related to the physical photon energy spectrum by

$$\frac{dN_\gamma(E)}{dE} = N_{stops}^{true} \cdot f_{capture} \cdot \epsilon_v \cdot \epsilon_{cs} \cdot \epsilon_{fp} \cdot \epsilon_c \cdot \epsilon_p \cdot \epsilon_{tr} \cdot \epsilon_{ph} \int dE_\gamma A(E_\gamma, E) \frac{d\Lambda(E_\gamma)}{dE_\gamma}, \tag{10}$$

where $f_{capture}$ is the fraction of muons that undergo OMC in the target. Its value for each nucleus has been measured previously [30] and is given in Table II. Integrating both sides of Eq. (10) over $E > 57$ MeV, and using Eqs. (5) and (9) gives the partial branching ratio in terms of observed photons and muon stops

$$R_\gamma = \frac{N^{obs}_{\gamma>57} \cdot F}{f_{capture} \cdot A_{av} \cdot N^{obs}_{stop} \cdot \kappa}. \tag{11}$$

The product of all efficiencies and correction factors is

$$\kappa = \epsilon_v \cdot \epsilon_{cs} \cdot \epsilon_{tr} \cdot \epsilon_{ph} \cdot \epsilon_{fp} \cdot \epsilon_c \cdot \epsilon_p \cdot C_{bm} \cdot C_{sim} \cdot C_o \cdot C_u \cdot C_m \cdot C_{md}. \tag{12}$$

If the Monte Carlo simulation exactly reproduces the spectrometer acceptance A_{av} then $N^{obs}_{stop} \cdot \kappa \cdot f_{capture}$ is the number of simulated photons which must originate in the target in order to produce the experimentally observed number of photons. The difference from unity of the calibration factor F indicates how well the acceptance was reproduced.

IV. RESULTS

A. Fits to the closure approximation polynomial

Results of the closure approximation analyses of nuclei from the present work are listed in Table III. Also included are results from Ref. [9] as well as recent results from a study of RMC on isotopes of Ni [31]. Quantities used in the calculation of R_γ (Eq. (11)) are given in the Appendix.

A comparison of closure RMC spectra to the observed RMC on O spectrum is shown in Fig. 5. The observed spectrum is typical of those obtained for other nuclei. The branching ratios obtained for Al, Si, and Ti are shown versus Z in Fig. 6 and versus neutron excess $\alpha = (N - Z)/A$ in Fig. 7. The Al and Si data reveal a $\sim 3\sigma$ difference between their R_γ values, confirming an earlier observation [9]. Similarly, R_γ for Ti was found to be $\sim 4\sigma$ smaller than an earlier value of R_γ for Ca which was measured using the same device [9]. Values of R_γ for Zr and Ag are also shown in Figs. 6 and 7. They are consistent with measurements of other nuclei of similar mass and fit into the generally decreasing trends of R_γ versus Z and α.

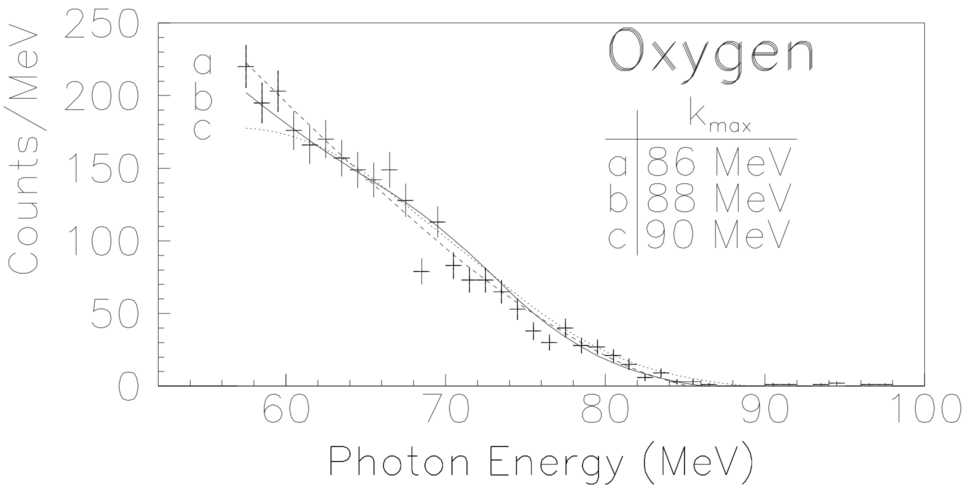

FIG. 5. Comparison of the experimental RMC on O photon spectrum (error bars) with the closure spectral shape of Eq. (7) after convolution with the spectrometer response and software cuts. The solid line is the spectral shape for the best fit value of k_{max}.

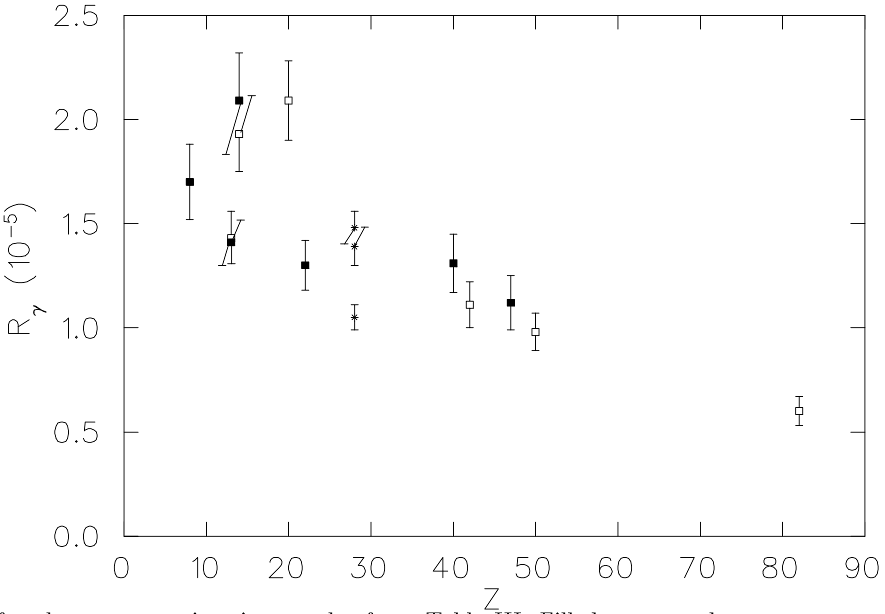

FIG. 6. R_γ vs. Z for closure approximation results from Table III. Filled squares show present results and open squares show the results of Ref. [9]. Stars indicate recent RMC on Ni results [31].

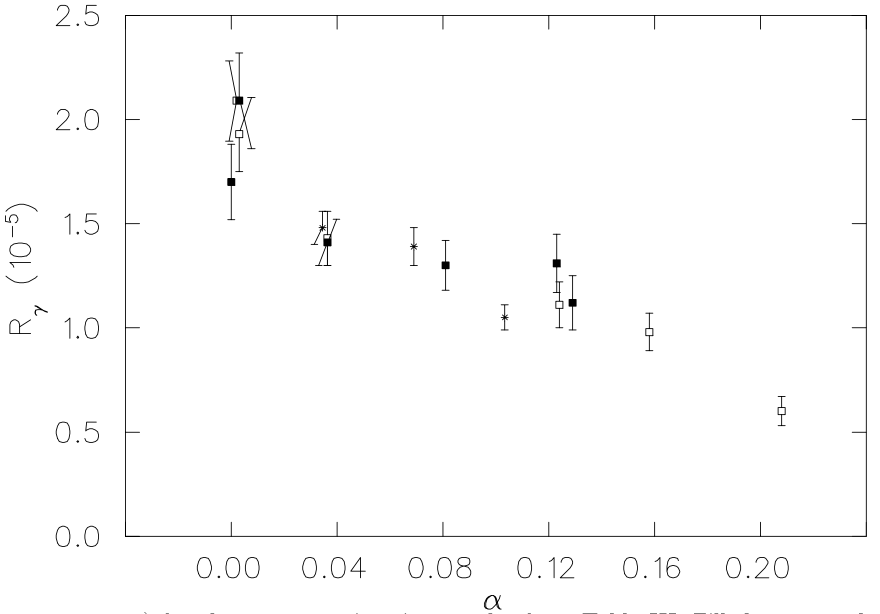

FIG. 7. R_γ vs. α (neutron excess) for closure approximation results from Table III. Filled squares show present results and open squares show the results of Ref. [9]. Stars indicate RMC on Ni results [31].

B. Fits to specific models

The integral method, described in section III E, was used in conjunction with specific nuclear RMC models in order to extract values of R_γ and g_p/g_a from experiment. The nuclear RMC amplitude is usually calculated in the impulse approximation (IA), which involves summing the elementary amplitude incoherently over all protons in the nucleus. The success of the IA requires that interactions involving two nucleons (via meson-exchange currents) are negligible. All but one of the nuclear RMC models employed here use this approximation in conjunction with an appropriate nuclear response.

Gmitro *et al.* [32] use a "modified impulse approximation" (MIA) by considering nucleon-nucleon interactions via meson-exchange currents (MEC) at the electromagnetic vertex. The MEC's are accounted for using constraints which follow from continuity of the electromagnetic current. A microscopic model (shell model) is used for the initial and final state nuclei. Theoretical predictions are similar to those of the semi-phenomenological "realistic" nuclear excitation model [33,34], which avoids the closure approximation by using giant dipole (GDR) and giant quadrupole (GQR) resonances for the final state nuclei.

Roig and Navarro [35] use SU(4) symmetry, a Hartree-Foch scheme for the target ground state, and sum rule techniques (which are particularly adapted to the analysis of inclusive processes) to calculate nuclear RMC. Due to the absence of RMC photon spectra, g_p is obtained here from the intersection of the theoretical R_γ vs. g_p curve with the value of R_γ as determined in the closure approximation.

Christillin *et al.* [29] avoid the closure approximation by using nuclear response functions calculated in a Fermi gas model. Nucleon-nucleon correlations are taken into account by introducing an effective nucleon mass M^* as a free parameter. The value of M^* ($M^* = 0.5M$) is fixed by fitting model-predicted OMC rates to experiment; the model then reproduces OMC rates to better than 10% for a large number of nuclei with $Z \geq 42$.

Fearing and Welsh have criticized the results of this approach and instead take a relativistic mean field theory approach in order to describe medium-to-heavy nuclei [36]. A relativistic Fermi gas model and a local density approximation, along with realistic nuclear density distributions, were used to relate the RMC process in infinite nuclear matter to finite nuclei. They predict RMC rates for light, medium, and heavy nuclei, but state that the theory is valid only for $Z \geq 20$. Also, the aim of this model was to assess the reliability with which g_p can be extracted from experimental data, rather than make explicit predictions. In fact, implementing the realistic nuclear density distributions results in RMC and OMC rates that are significantly higher than the experimental values.

Three calculations of RMC on O [32,33,35] are available for direct comparison with experiment. However no nuclear responses have been calculated for Al, Si, Ti, Zr or Ag. In the absence of such calculations, the naive assumption that the nuclear response for Ti is similar to that for Ca, was made. In this case, three calculations of the nuclear RMC response in Ca [32,34,35] are available for use in the extraction of R_γ and g_p from the Ti data. Under a similar assumption the calculated nuclear RMC responses of Mo and Sn [29] were substituted for those of Zr and Ag, respectively, before R_γ and g_p values were determined from the Zr and Ag data. Because no calculations of RMC exist for nuclei nearby in Z, g_p was not extracted from the Al or Si data using the integral method. The integral method results for R_γ and g_p/g_a for O, Ti, Zr and Ag are listed in Table IV along with previous results from other nuclei.

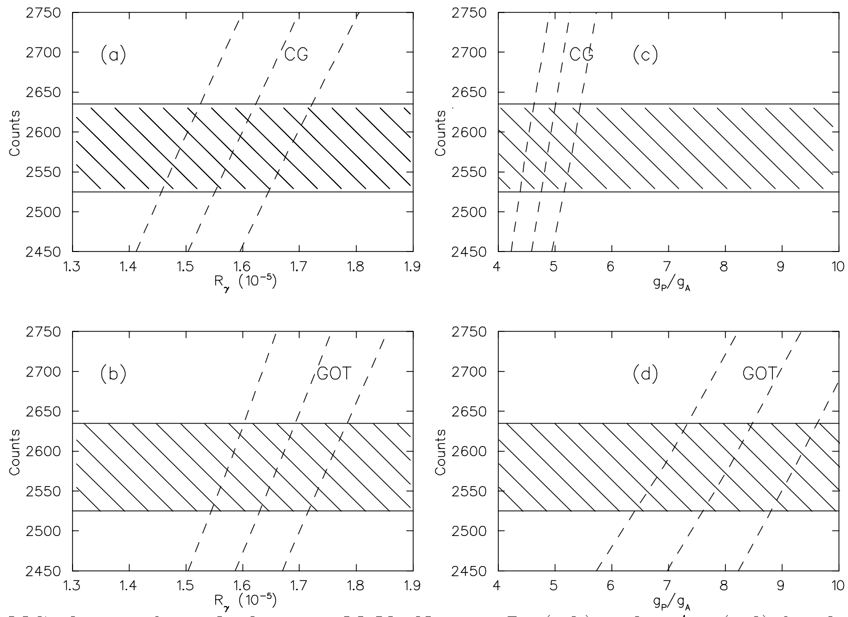

FIG. 8. Number of RMC photons from O above 57 MeV, N_γ, vs. R_γ (a,b) and g_p/g_a (c,d) for the RMC on O theories of Gmitro *et al.* (GOT) [32] and Christillin and Gmitro (CG) [33]. The solid lines denote the error band on the number of RMC photons after subtraction of background. The middle dashed curve in each plot is the theoretical prediction and the dashed curves on either side indicate the error in the prediction due to uncertainties in acceptance and stopping distribution.

Values of R_γ and g_p/g_a, obtained for O using the integral method, were read directly from Fig. 8. Values of R_γ and g_p/g_a for Ti, Zr, and Ag were obtained from similar figures. A comparison of the measured RMC on O photon spectrum to the simulated spectra obtained using the theory of Gmitro et al. and various values of g_p/g_a, is shown in Fig. 9. A similar comparison is made in Fig. 9 using the theory of Christillin and Gmitro.

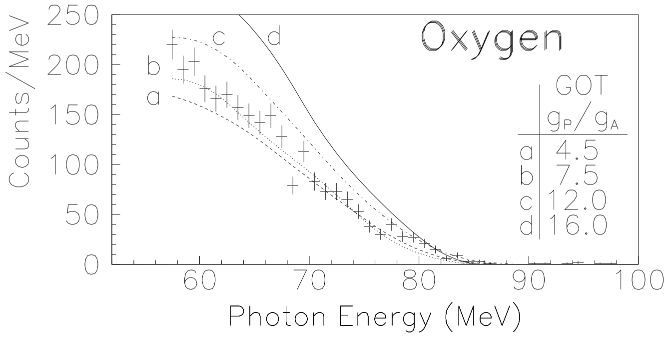

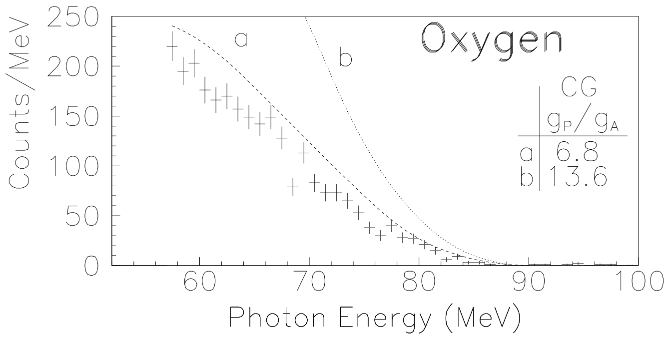

FIG. 9. Comparison of the experimental RMC on O photon spectrum with the theories of Gmitro *et al.* (GOT) [32] and Christillin and Gmitro (CG) [33]. The theoretical spectra have undergone Monte Carlo convolution and software cuts, and have been normalized to reflect the results in Fig. 8.

V. DISCUSSION

A. Trends in R_γ

The present set of R_γ measurements, combined with previous measurements using the same spectrometer, exhibit three features. The closure approximation branching ratios for the neighboring nuclei, Al (1.41 ± 0.11) and Si (2.09 ± 0.23) (units 10^{-5}), differ significantly, suggesting that R_γ is not a smooth function of Z. This result confirms earlier measurements of the same nuclei [9]. A similar effect was observed for the first time in the near-neighbor nuclei Ca (2.09 ± 0.19) and Ti (1.30 ± 0.12) (units 10^{-5}). These two features appear to be due specifically to the RMC part of R_γ because the OMC branching ratio changes by 8% or less within each pair of nuclei (see Table II). The third feature is a suppression of R_γ in the nuclei Zr and Ag, which confirms a trend observed earlier for heavy nuclei [9]. This trend also appears to be an RMC effect because the OMC branching ratios are nearly independent of Z and neutron excess for medium and heavy nuclei.

In all three effects an increase in the neutron excess is accompanied by a decrease in R_γ, indicating that Pauli blocking of the final state neutron might be responsible. However, R_γ is the ratio of RMC to OMC branching ratios and Pauli blocking reduces the available phase space for both reactions. Additional suppression of RMC relative to OMC is due to the extra final state particle in the RMC reaction which further reduces phase space. If neutron phase space and Pauli blocking are the responsible mechanisms, then R_γ as a function of the neutron excess α, rather than Z, should show the clearer trend. A comparison of Figs. 6 and 7 supports this assertion, with more nuclei lying close to the decreasing trend line in α than in Z. The present results, indicating that R_γ is not a smooth function of Z and that it is a much smoother function of the neutron excess α, confirm and extend the conclusions of an earlier study of the neutron excess effect in nickel isotopes [31].

Theoretical predictions of R_γ vs. α are compared to previous and present closure approximation results in Figs. 10 and 11. In Fig. 10, the theory of Christillin *et al.* [29] agrees well with the experimental R_γ vs. α plot for $\alpha > 0.01$ and $g_p/g_a = 0$. The theories of Christillin [34] and Christillin and Gmitro [33] are included for comparison with the low Z results where there is agreement between experiment and theory for the $g_p/g_a = 6.8$ curve. In Fig. 11, the theory of Fearing and Welsh [36] reproduces the shape of the experimental R_γ vs. α plot for $\alpha > 0.01$, but only after the theoretical values of R_γ are scaled by ~ 0.4. Comparison between theory and experiment for $Z < 20$ is included in the figure, but the Fearing and Welsh model is not expected to be applicable for these nuclei.

B. Oxygen

The experimental and theoretical situation for O is summarized by the values of R_γ and g_p/g_a listed in Table IV. The first two measurements of the RMC rate in O were motivated by the hope that g_p/g_a could be reliably extracted and therefore provide a test of PCAC in nuclei. Both results were analyzed using the theory of Christillin and Gmitro [33]; one [10] led to a value of g_p/g_a consistent with the PCAC predicted value (0.9 σ above it), while the other [14] led to a value 4.5 σ above the PCAC prediction. A subsequent measurement of R_γ [8], which agreed with that of Ref. [10], was analyzed using two different theories. One theory [33] produced a value of g_p/g_a 0.7 σ above PCAC and consistent with the measurement of Ref. [10]. The other [32] produced a much higher value 4 σ above the PCAC prediction. The consistently high values of g_p/g_a led to speculation that nuclear medium effects might cause an effective increase in g_p. The strong model dependence led to doubt that g_p/g_a could be reliably extracted from nuclear RMC.

The present values of R_γ are about 30% smaller than those of Refs. [10] and [8]. The difference with the latter measurement may be due to a rate effect error which was absent in the present detector. The three theories used to analyze the present O data produce g_p/g_a values in reasonable agreement with the PCAC and chiral perturbation theory values. Two theories [32,35] yielded values of g_p/g_a consistent with PCAC (+0.9 σ and -0.3 σ, respectively), and one [33] yielded a value which was low (-3.6 σ). These results display only a small model dependence and increase confidence in the extracted value of g_p/g_a. The nearness of g_p/g_a to its PCAC value indicates that it is unnecessary to invoke the nuclear medium effects that were used to explain the larger values of earlier results.

C. Trends in g_p/g_a

The g_p/g_a results of the integral method analyses, listed in Table IV, are plotted versus atomic number in Fig. 12. The present values confirm a downward trend in g_p/g_a versus Z, with nearly all medium to heavy nuclei having values well below the PCAC value. A downward trend is expected because R_γ also decreases with Z, but a detailed explanation of this behavior is beset with several problems. The first of these is the scarcity of detailed calculations of RMC in all but the lightest nuclei. For example, the g_p/g_a values for Ti had to be calculated using the nuclear response of Ca, assuming that Ca and Ti are similar. This assumption appears to be invalid, at least with respect to RMC, when one considers the large difference in their R_γ values. For nuclei with $Z \geq 40$, the g_p/g_a values were determined using only the Fermi gas model of Christillin *et al.* [29].

Another problem is that while general trends in g_p/g_a can be reproduced, a consistent set of absolute values is difficult to obtain. In Christillin's Fermi gas model, the observed decrease of g_p/g_a and R_γ with increasing Z arises from a quenching of g_p with Z. However, the values of g_p/g_a required to reproduce the experimental R_γ's (see Table IV) do not agree with the values of g_p/g_a required to reproduce the well-known OMC rates [30].

Fearing and Welsh [36] were also able to reproduce the shape of the R_γ versus α plot for $Z > 20$, but without the requirement of a Z-dependent quenching of g_p. However, their values of R_γ are roughly 2.5 times larger than experimental values, assuming the PCAC value of g_p. They also find that R_γ is quite sensitive to various inputs in the Fermi gas model, which suggests that it is difficult to extract values of g_p in this model.

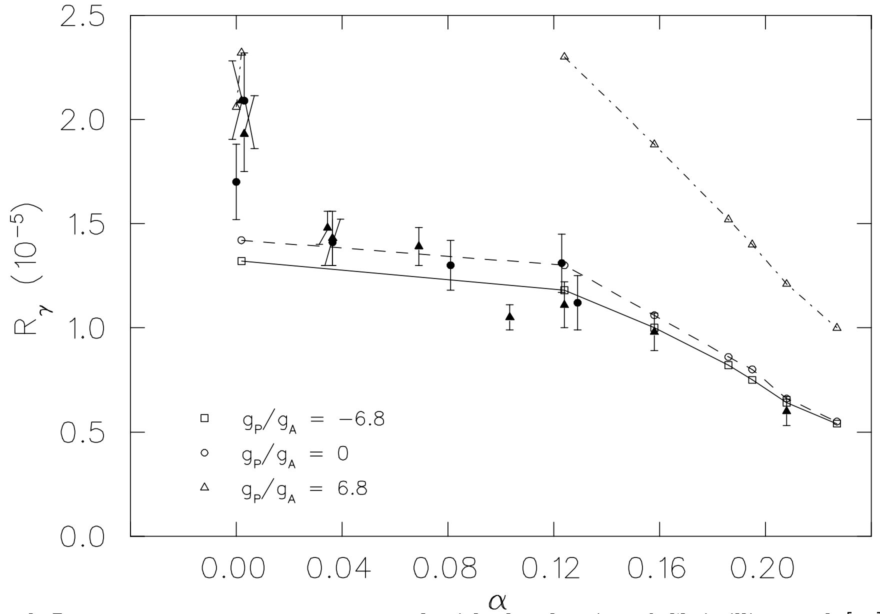

FIG. 10. Experimental R_γ vs. neutron excess α compared with the theories of Christillin *et al.* [29] ($Z \geq 40$), Christillin [34] ($Z = 20, \alpha = 0.00195$), and Christillin and Gmitro [33] ($Z = 8, \alpha = 0$). Experimental values of R_γ are shown by the solid circles (present closure approximation results) and solid triangles (previous closure approximation results [9,31]), and are taken from Table III. Theoretical values are shown by open squares, circles and triangles connected by lines to guide the eye.

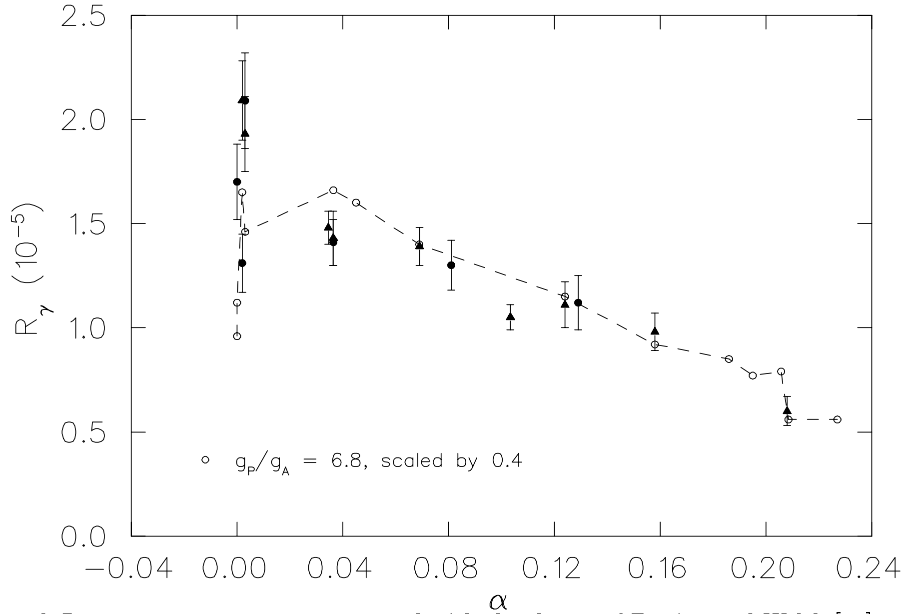

FIG. 11. Experimental R_γ vs. neutron excess α compared with the theory of Fearing and Welsh [36], scaled by 0.4. Theoretical values of R_γ for $Z < 20$ are shown even though this model is not expected to apply to such nuclei. Experimental values of R_γ are shown by the filled circles (present closure approximation results) and filled triangles (previous closure approximation results [9,31]), and are taken from Table III. Theoretical values are shown by open circles connected by a dashed line to guide the eye.

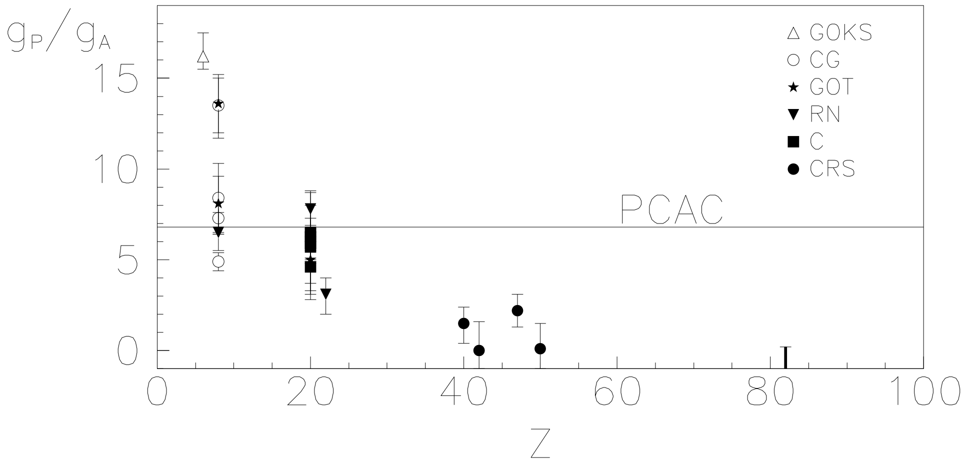

FIG. 12. g_p/g_a as a function of atomic number. Plotted values are from Table IV (integral method results). The acronyms in the symbol legend correspond to the different theoretical models used to extract g_p/g_a, which are given in full in the caption to Table IV.

D. RMC in Ti as a Background to $\mu - e$ Conversion

RMC is a major background for $\mu - e$ conversion experiments, many of which use Ti as a target [37]. This background arises from the asymmetric conversion of RMC photons in which a high-energy positron is produced. Before now, RMC on Ti had never been measured so the experimental branching ratio for Ca was used, corrected by a factor of 0.91 to account for the Z-dependence of the RMC to OMC ratio. A Primakoff polynomial spectral shape was assumed and applied to each Ti isotope. The end-point photon energy for each isotope was determined by subtracting from the kinematical RMC endpoint the same amount subtracted in the Ca case. This was found not to be sufficient to describe the observed background, so an additional spectrum with a 93 MeV endpoint was added.

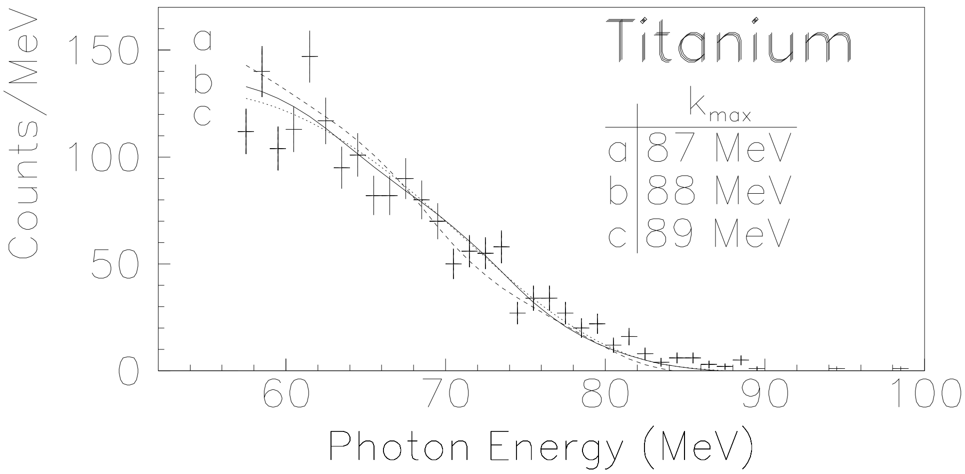

FIG. 13. Comparison of the experimental RMC on Ti photon spectrum (error bars) with the closure spectral shape of Eq. (7) after convolution with the spectrometer response and software cuts. The solid line is the spectral shape for the best fit value of k_{max}.

The measured RMC in Ti rate ($R_\gamma = 1.30 \times 10^{-5}$) is lower than the 1.93×10^{-5} assumed in Ref. [37]. Also, the best fit of the end-point energy k_{max} to the spectrum was 88.1 MeV, a bit lower than the assumed value of 89.7 MeV for the dominant Ti isotope. As shown in Fig. 13, there appears to be no evidence of RMC photons between 88 and 93 MeV.

VI. CONCLUSIONS

Values of R_γ, the ratio of the radiative muon capture rate for photon energies > 57 MeV to the rate of ordinary muon capture, have been measured in six nuclei: O, Al, Si, Ti, Zr, and Ag. The observed rate differences between the nearby nuclei Ti and Ca and between Al and Si confirm the observation that R_γ is not a smooth function of Z [9]. The rates for Zr and Ag confirm the suppression of RMC relative to OMC in heavy nuclei [9]. The present set of rate measurements, combined with measurements on specific isotopes [31], suggest that R_γ is a smooth, decreasing function of the neutron excess α, which in turn suggests that Pauli blocking of the final state neutron is relatively more important in RMC than in OMC.

Three different theories, each of which included detailed treatments of the nuclear response, were used to obtain values of g_p/g_a from the measured RMC rate in O. These were 4.9 ± 0.5 [33], $8.1^{+1.5}_{-1.7}$ [32], and $6.4^{+1.0}_{-1.1}$ [35]. Two of the three resulting values are consistent with the PCAC prediction of 6.7. The fair or good agreement of the three values among themselves indicated a much smaller model dependence than observed in earlier studies and led to greater confidence that meaningful values of g_p/g_a can be extracted from RMC in light nuclei. The agreement with PCAC makes it unlikely that nuclear medium effects need to be invoked for light nuclei, as they were to explain earlier, larger values of g_p/g_a.

Present values of g_p/g_a for other nuclei confirm a downward trend versus Z, with nearly all medium to heavy nuclei having values well below the PCAC value. However, the g_p/g_a values are suspect in most such nuclei because detailed calculations of RMC for them do not exist. In the Fermi gas model of Christillin *et al.* [29], the suppression of g_p/g_a is due to a quenching of g_p with Z, but the relativistic Fermi gas model of Fearing and Welsh [36], which reproduces trends in R_γ as a function of Z and α, does not require such quenching.

The measurement of the RMC rate and spectrum shape in Ti should prove useful in the determination of a major backgound in $\mu - e$ conversion experiments. The present value of $R_\gamma = (1.30 \pm 0.12) \times 10^{-5}$ is 33% lower than that assumed in a recent experiment [37]. In addition no RMC photons were observed with energies between 88 and 93 MeV.

ACKNOWLEDGMENTS

The authors wish to thank D. Sample and N.S. Zhang for their assistance during this experiment. This work was supported by the National Research Council and the Natural Sciences and Engineering Research Council of Canada and the U.S. National Science Foundation.

APPENDIX: CALCULATED QUANTITIES

The quantities in Table V were used to determine R_γ and g_p/g_a for O, Al, Si, Ti, Zr, and Ag. $N^{obs}_{\gamma>57}$ is the observed number of photons (> 57 MeV) after all software cuts, but before the removal of the empty target background in the cases of O and Si. The error in this value is the quadrature sum of the counting statistics and a 0.3 MeV uncertainty in the photon energy calibration. N^{obs}_{stops} is the number of muons passing through the beam counters. See section III, subsections C, D, and E for details on all quantities.

---

[1] E. Fermi, Z. Physik **88**, 161 (1934); E. Fermi, Nuov. Cim. **11**, 1 (1934).
[2] L. Grenacs, Annu. Rev. Nucl. Part. Sci. **35**, 455 (1985).
[3] S.L. Adler and Y. Dothan, Phys. Rev. **151**, 1267 (1966).

[4] L. Wolfenstein, *High-Energy Physics and Nuclear Structure*, edited by S. Devons (Plenum, New York, 1970), p.661.
[5] V. Bernard, N. Kaiser, and Ulf-G. Meissner, Phys. Rev. D **50**, 6899 (1994).
[6] G. Jonkmans, S. Ahmad, D.S. Armstrong, G. Azuelos, W. Bertl, M. Blecher, C.Q. Chen, P. Depommier, B.C. Doyle, T. von Egidy, T.P. Gorringe, P. Gumplinger, M.D. Hasinoff, D. Healey, A.J. Larabee, J.A. Macdonald, S.C. McDonald, M. Munro, J.-M. Poutissou, R. Poutissou, B.C. Robertson, D.G. Sample, E. Saettler, C.N. Sigler, G.N. Taylor, D.H. Wright, and N.S. Zhang, Phys. Rev. Lett. **77**, 4512 (1996).
[7] D.H. Wright, S. Ahmad, D.S. Armstrong, G. Azuelos, W. Bertl, M. Blecher, C.Q. Chen, P. Depommier, B.C. Doyle, T. von Egidy, T.P. Gorringe, P. Gumplinger, M.D. Hasinoff, D. Healey, G. Jonkmans, A.J. Larabee, J.A. Macdonald, S.C. McDonald, M. Munro, J.-M. Poutissou, R. Poutissou, B.C. Robertson, D.G. Sample, E. Saettler, C.N. Sigler, G.N. Taylor, and N.S. Zhang, Phys. Rev. C **57**, 373 (1998).
[8] D.S. Armstrong, S. Ahmad, R.A. Burnham, T.P. Gorringe, M.D. Hasinoff, A.J. Larabee, C.E. Waltham, G. Azuelos, J.A. Macdonald, T. Numao, J-M. Poutissou, M. Blecher, D.H. Wright, E.T.H. Clifford, J. Summhammer, P. Depommier, R. Poutissou, H. Mes, and B.C. Robertson, Phys. Rev. C **43**, 1425 (1991).
[9] D.S. Armstrong, A. Serna-Angel, S. Ahmad, G. Azuelos, W. Bertl, M. Blecher, C.Q. Chen, P. Depommier, T. von Egidy, T.P. Gorringe, M.D. Hasinoff, R.S. Henderson, A.J. Larabee, J.A. Macdonald, S.C. McDonald, J-M. Poutissou, R. Poutissou, B.C. Robertson, D.G. Sample, G.N. Taylor, D.H. Wright, and N.S. Zhang, Phys. Rev. C **46**, 1094 (1992).
[10] M. Döbeli, M. Doser, L. van Elmbt, M.W. Schaad, P. Truöl, A. Bay, J.P. Perroud, J. Imazato, and T. Ishikawa, Phys. Rev. C **37**, 1633 (1988).
[11] R.D. Hart, C.R. Cox, G.W. Dodson, M. Eckhause, J.R. Kane, M.S. Pandey, A.M. Rushton, R.T. Siegel, and R.E. Welsh, Phys. Rev. Lett. **39**, 399 (1977).
[12] A. Frischknecht, W. Stehling, G. Strassner, P. Truöl, J.C. Alder, C. Joseph, J.F. Loude, J.P. Perroud, D. Ruegger, T.M. Tran, W. Dahme, H. Panke, and R. Kopp, Phys. Rev. C **32**, 1506 (1985).
[13] C.J. Virtue, Ph.D. thesis, University of British Columbia, 1987 (unpublished).
[14] A. Frischknecht, M. Döbeli, W. Stehling, G. Strassner, P. Truöl, J.C. Alder, C. Joseph, J.F. Loude, J.P. Perroud, D. Ruegger, M.T. Tran, and H. Panke, Phys. Rev. C **38**, 1996 (1988).
[15] TRIUMF Users Executive Committee, *TRIUMF Users Handbook* Technical Report, TRIUMF, 1988.
[16] D.H. Wright, S. Ahmad, D.S. Armstrong, G. Azuelos, W. Bertl, M. Blecher, C.Q. Chen, T.P. Gorringe, M.D. Hasinoff, R.S. Henderson, J.A. Macdonald, J-M. Poutissou, R. Poutissou, B.C. Robertson, D.G. Sample, A. Serna-Angel, G. Taylor, and N.S. Zhang, Nucl. Instrum. Methods Phys. Res. A **320**, 249 (1992).
[17] R. MacDonald, D.S. Beder, D. Berghofer, M.D. Hasinoff, D.F. Measday, M. Salomon, J. Spuller, T. Suzuki, J-M. Poutissou, R. Poutissou, P. Depommier, and J.K.P. Lee, Phys. Rev. Lett. **38**, 746 (1977).
[18] CERN Application Software Group. *GEANT – Detector Description and Simulation Tool*, CERN Program Library Long Writeup W5013, Geneva, 1993.
[19] C. Kost and P. Reeve. *REVMOC, A Monte Carlo Beam Transport Program.* Paper presented at the EPS Conference on Computing in Accelerator Design and Operation, Berlin, 1983.
[20] J.P. Perroud, A. Perrenoud, J.C. Alder, B. Gabioud, C. Joseph, J.F. Loude, N. Morel, M.T. Tran, E. Windlemann, H. Von Fellenberg, G. Strassner, P. Truöl, W. Dahme, H. Panke, and D. Renker, Nucl. Phys. **A453**, 542 (1986).
[21] J.A. Bistirlich, K.M. Crowe, A.S.L. Parsons, P. Skarek, and P. Truöl, Phys. Rev. C **5**, 1867 (1972).
[22] H.P.C. Rood and H.A. Tolhoek, Nucl. Phys. **70**, 658 (1965).
[23] H.P.C. Rood, A.F. Yano, and F.B. Yano, Nucl. Phys. **A228**, 333 (1974).
[24] H.W. Fearing, Phys. Rev. **146**, 723 (1966).
[25] R.S. Sloboda and H.W. Fearing, Nucl. Phys. **A340**, 342 (1980).
[26] R.S. Sloboda and H.W. Fearing, Phys. Rev. C **18**, 2265 (1978).
[27] E. Borchoi and S. De Gennaro, Phys. Rev. C **2**, 1012 (1970).
[28] H. Primakoff, Rev. Mod. Phys. **31**, 802 (1959).
[29] P. Christillin, M. Rosa-Clot, and S. Servadio, Nucl. Phys. **A345**, 331 (1980).
[30] T. Suzuki, D.F. Measday and J.P. Roalsvig, Phys. Rev. C **35**, 2212 (1987).
[31] T.P. Gorringe, D.S. Armstrong, C.Q. Chen, E. Christy, B.C. Doyle, P. Gumplinger, H.W. Fearing, M.D. Hasinoff, M.A. Kovash, and D.H. Wright, Phys. Rev. C **58**, 1767 (1998).
[32] M. Gmitro, A.A. Ovchinnikova, and T.V. Tetereva, Nucl. Phys. **A453**, 685 (1986).
[33] P. Christillin and M. Gmitro, Phys. Lett. **150B**, 50 (1985).
[34] P. Christillin, Nucl. Phys. **A362**, 391 (1981).
[35] F. Roig and J. Navarro, Phys. Lett. B **236**, 393 (1990).
[36] H.W. Fearing and M.S. Welsh, Phys. Rev. C **46**, 2077 (1992).
[37] J. Kaulard, C. Dohmen, H. Haan, W. Honecker, D. Junker, G. Otter, M. Starlinger, P. Wintz, J. Hofmann, W. Bertl, J. Egger, B. Krause, S. Eggli, R. Engfer, Ch. Findeisen, E.A. Hermes, T. Kozlowski, C.B. Niebuhr, M. Rutsche, H.S. Pruys, and A. van der Schaaf, Phys. Lett. B **422**, 334 (1998).

TABLE I. Dimensions of RMC targets. All targets were mounted perpendicular to the beam axis.

Target	Shape	Dimensions	No. of foils	Spacing of foils
O	disk	14.4 cm dia. $\times$ 3.0 cm thick	1	–
Al	disk	8.5 cm dia. $\times$ 0.15 cm thick	10	0.87 cm
Si	disk	8.6 cm dia. $\times$ 2.0 cm thick	1	–
Ti	disk	15.5 cm dia. $\times$ 20.0 cm thick	1	–
Zr	square	10.0 cm $\times$ 10.0 cm $\times$ 0.025 cm	15	0.69 cm
Ag	square	10.0 cm $\times$ 10.0 cm $\times$ 0.037 cm	7	0.96 cm

TABLE II. OMC capture fractions and mean muon capture lifetimes in nuclear targets [30].

nucleus	$f_{capture}$	τ (ns)
O	0.1844 ± 0.0009	1795.4 ± 2.0
Al	0.6095 ± 0.0005	864.0 ± 1.0
Si	0.6587 ± 0.0005	756.0 ± 1.0
Ca	0.8508 ± 0.0007	332.7 ± 1.5
Ti	0.8530 ± 0.0006	329.3 ± 1.3
Zr	0.9529 ± 0.0004	110.0 ± 1.0
Ag	0.9634 ± 0.0006	87.0 ± 1.5

TABLE III. Values of R_γ, k_{max}, and the corresponding χ^2 of fit as determined by the shape method (closure approximation). $\alpha = (N-Z)/A$ is the neutron excess, where A is the atomic mass of the natural element, and $N = A - Z$.

	Z	α	R_γ (10^{-5})	k_{max} (MeV)	χ^2/d.o.f.	Reference
O	8	0	1.67 ± 0.17	87.1 ± 1.9	1.5	a
Al	13	0.0364	1.41 ± 0.11	88.5 ± 1.2	1.6	a
			1.43 ± 0.13	90 ± 2	1.1	b
Si	14	0.00304	2.09 ± 0.23	87.8 ± 1.7	1.9	a
			1.93 ± 0.18	92 ± 2	1.7	b
Ca	20	0.00195	2.09 ± 0.19	93 ± 2	1.6	b
Ti	22	0.0810	1.30 ± 0.12	88.1 ± 2.0	1.4	a
^{58}Ni	28	0.0345	1.48 ± 0.08	92 ± 2	1.8	c
^{60}Ni	28	0.0690	1.39 ± 0.09	90 ± 2	2.0	c
^{62}Ni	28	0.1034	1.05 ± 0.06	89 ± 2	1.3	c
Zr	40	0.123	1.31 ± 0.14	87.1 ± 2.0	1.3	a
Mo	42	0.124	1.11 ± 0.11	90 ± 2	0.8	b
Ag	47	0.129	1.12 ± 0.13	87.3 ± 1.9	1.0	a
Sn	50	0.158	0.98 ± 0.09	87 ± 2	1.1	b
Pb	82	0.208	0.60 ± 0.07	84 ± 3	0.8	b

[a] Denotes the results of this experiment.
[b] Denotes the results of Ref. [9].
[c] Denotes the results of Ref. [31].

TABLE IV. Values of g_p/g_a and R_γ as determined by the integral method. "CG" refers to Christillin and Gmitro [33]; "GOT" refers to Gmitro *et al.* [32]; "RN" refers to Roig and Navarro [35]; "C" refers to Christillin [34]; and "CRS" refers to Christillin *et al.* [29].

	Z	g_p/g_a	R_γ (10^{-5})	Theory	Experiment
O	8	13.5 ± 1.5	3.8 ± 0.4	CG	g
		8.4 ± 1.9	2.44 ± 0.47	CG	d
		7.3 ± 0.9	2.22 ± 0.23	CG	c
		$13.6^{+1.6}_{-1.9}$	2.18 ± 0.21	GOT	c
		4.9 ± 0.5	$1.58^{+0.14}_{-0.12}$	CG	a
		$8.1^{+1.5}_{-1.7}$	1.66 ± 0.12	GOT	a
		$6.4^{+1.0}_{-1.1}$	1.67 ± 0.17	RN	a
Ca	20	4.6 ± 0.9	1.96 ± 0.20	C	e
		6.5 ± 1.5	$2.35^{+0.32}_{-0.30}$	C	f
		$6.0^{+2.8}_{-2.9}$	$2.15^{+0.27}_{-0.26}$	GOT	f
		5.9 ± 0.8	2.21 ± 0.15	C	b
		5.0 ± 1.7	2.07 ± 0.14	GOT	b
		7.8 ± 0.9	2.09 ± 0.19	RN	b
		$6.3^{+1.0}_{-1.5}$	2.30 ± 0.21	C	d
		5.7 ± 0.8	2.18 ± 0.16	C	c
		$4.6^{+1.7}_{-1.8}$	2.04 ± 0.14	GOT	c
Ti	22	< 0	$1.26^{+0.09}_{-0.08}$	C	a
		< 0	$1.46^{+0.06}_{-0.05}$	GOT	a
		$3.1^{+0.9}_{-1.1}$	1.30 ± 0.12	RN	a
Zr	40	$1.5^{+0.9}_{-1.1}$	$1.40^{+0.13}_{-0.11}$	CRS	a
Mo	42	$0.0^{+1.6}_{-4.1}$	1.26 ± 0.10	CRS	b
Ag	47	2.2 ± 0.9	$1.21^{+0.11}_{-0.10}$	CRS	a
Sn	50	$0.1^{+1.4}_{-7.5}$	1.03 ± 0.08	CRS	b
Pb	82	< 0.2	0.60 ± 0.05	CRS	b

[a] Denotes the results of this experiment.
[b] Denotes the results of Ref. [9].
[c] Denotes the results of Ref. [8].
[d] Denotes the results of Ref. [10].
[e] Denotes the results of Ref. [12].
[f] Denotes the results of Ref. [13].
[g] Denotes the results of Ref. [14].

TABLE V. Quantities used to determine R_γ and g_p/g_a for O, Al, Si, Ti, Zr, and Ag.

	O	Al	Si
$N^{obs}_{\gamma>57}$	2637 ± 51	3051 ± 55	3302 ± 57
N^{obs}_{stops}	1.299×10^{11}	5.410×10^{10}	4.011×10^{10}
ϵ_v	0.9613 ± 0.0006	0.9705 ± 0.0010	0.9730 ± 0.0010
ϵ_{cs}	0.976 ± 0.005	0.976 ± 0.005	0.976 ± 0.005
ϵ_{fp}	0.945 ± 0.005	0.966 ± 0.005	0.970 ± 0.005
ϵ_c	0.958 ± 0.002	0.949 ± 0.004	0.942 ± 0.005
ϵ_p	0.940 ± 0.013	0.927 ± 0.009	0.910 ± 0.007
C_{bm}	1.022 ± 0.004	1.019 ± 0.003	1.019 ± 0.002
C_{sim}	0.99558 ± 0.00004	0.99788 ± 0.00002	0.9771 ± 0.0002
C_o	0.987 ± 0.003	0.991 ± 0.002	0.9901 ± 0.0016
C_u	1.007 ± 0.002	1.0064 ± 0.0019	1.0053 ± 0.0013
C_m	1.026 ± 0.005	1.022 ± 0.004	1.021 ± 0.003
C_{md}	1.0024 ± 0.0003	1.0012 ± 0.0002	1.0014 ± 0.0003
f_{empty}	0.022 ± 0.007	—	0.046 ± 0.013
$A_{av} \cdot \epsilon_{tr} \cdot \epsilon_{ph}$	0.0073 ± 0.0006	0.0074 ± 0.0004	0.0067 ± 0.0006
F	0.94 ± 0.05	0.94 ± 0.05	0.94 ± 0.05

	Ti	Zr	Ag
$N^{obs}_{\gamma>57}$	1785 ± 42	952 ± 31	811 ± 28
N^{obs}_{stops}	2.689×10^{10}	1.499×10^{10}	1.570×10^{10}
ϵ_v	0.908 ± 0.003	0.912 ± 0.004	0.913 ± 0.005
ϵ_{cs}	0.976 ± 0.005	0.976 ± 0.005	0.976 ± 0.005
ϵ_{fp}	0.981 ± 0.005	0.983 ± 0.002	0.985 ± 0.004
ϵ_c	0.954 ± 0.006	0.934 ± 0.003	0.927 ± 0.007
ϵ_p	0.869 ± 0.011	0.78 ± 0.03	0.758 ± 0.017
C_{bm}	1.022 ± 0.006	1.0208 ± 0.0014	1.15 ± 0.05
C_{sim}	0.98131 ± 0.00018	0.9597 ± 0.0004	0.9682 ± 0.0003
C_o	0.988 ± 0.002	0.9887 ± 0.0010	0.983 ± 0.011
C_u	1.017 ± 0.005	1.0117 ± 0.0011	1.008 ± 0.009
C_m	1.030 ± 0.010	1.0300 ± 0.0017	1.017 ± 0.013
C_{md}	1.0003 ± 0.0002	1.0004 ± 0.0002	1.0003 ± 0.0002
f_{empty}	—	—	—
$A_{av} \cdot \epsilon_{tr} \cdot \epsilon_{ph}$	0.0075 ± 0.0005	0.0074 ± 0.0006	0.0065 ± 0.0005
F	0.94 ± 0.05	0.94 ± 0.05	0.94 ± 0.05